The Astronomical Journal, 159:209 (13pp), 2020 May https://doi.org/10.3847/1538-3881/ab7faf

Hubble Space Telescope Search for Activity in High-perihelion Objects

Jing Li (李京)[1], David Jewitt[1,2], Max Mutchler[3], Jessica Agarwal[4], and Harold Weaver[5]
[1] Department of Earth, Planetary and Space Sciences, UCLA, 595 Charles Young Drive East, Los Angeles, CA 90095-1567, USA; jli@igpp.ucla.edu
[2] Department of Physics and Astronomy, UCLA, 430 Portola Plaza, Box 951547, Los Angeles, CA 90095-1547, USA
[3] Space Telescope Science Institute, 3700 San Martin Drive, Baltimore, MD 21218, USA
[4] Max Planck Institute for Solar System Research, Justus-von-Liebig-Weg 3, D-37077 Göttingen, Germany
[5] The Johns Hopkins University Applied Physics Laboratory, 11100 Johns Hopkins Road, Laurel, MD 20723, USA
Received 2020 January 17; revised 2020 March 10; accepted 2020 March 11; published 2020 April 14

Abstract

Solar system objects with perihelia beyond the orbit of Jupiter ($q > 5$ au) are too cold for water ice to generate an appreciable coma via sublimation. Despite this, numerous high-perihelion objects (HPOs) including many comets and recently escaped Kuiper Belt objects (Centaurs) are observed to be active out at least to the orbit of Saturn ($q \sim 10$ au). Peak equilibrium temperatures at 10 au (∼125 K), while far too low to sublimate water ice, are sufficient to sublimate supervolatiles such as CO and CO_2 ice. Temperatures at 10 au are also high enough to trigger the rapid crystallization of exposed amorphous ice, thus constituting another possible driver of distant activity. While supervolatile ices can sublimate strongly (as r_H^{-2}) to at least Kuiper Belt (30 au) distances, crystallization is an exponential function of temperature that cannot be sustained much beyond ∼10 au. The heliocentric dependence of the activity thus suggests an observational test. If activity in high-perihelion objects is triggered by crystallization, then no examples of activity should be found with perihelia of $q \gg 10$ au. If, on the other hand, activity is due to free sublimation of exposed supervolatile ices, or another cause, then distant activity might be detected. We obtained sensitive, high-resolution Hubble Space Telescope observations of HPOs to search for activity beyond the crystallization zone. No examples of activity were detected in 53 objects with $q > 15$ au, consistent with the crystallization trigger hypothesis. However, sensitivity limits are such that we cannot reject the alternative hypothesis that mass loss is driven by the sublimation of supervolatile ices. We also searched for binary companions in our sample, finding none and setting an empirical 3σ limit to the binary fraction of <8%.

Unified Astronomy Thesaurus concepts: Minor planets (1065); Comets (280); Small solar system bodies (1469); Centaurs (215)

1. Introduction

The Kuiper bBelt is a vast solar system repository located beyond Neptune, containing billions of ice-rich objects larger than 1 km and having a combined mass $\lesssim 0.1\,M_\oplus$ (Earth mass $M_\oplus = 6.0 \times 10^{24}$ kg). The belt is a relic of the formation epoch, and a reservoir holding some of the least thermally processed material in the solar system. Some Kuiper Belt objects are dynamically unstable on billion-year timescales, causing them to drift into planet-approaching orbits and hence to be scattered across the solar system. In particular, the Neptune-approaching "scattered disk" component of the Kuiper Belt (prototype object 1996 TL66; Luu et al. 1997) is the probable source region from which most objects escape (Volk & Malhotra 2008). Some escaped Kuiper Belt objects diffuse into orbits interior to that of Jupiter (semimajor axis $a_J = 5.203$ au, eccentricity $e_J = 0.048$, and perihelion and aphelion distances of 4.953 au and 5.453 au, respectively) where the equilibrium radiation temperatures are sufficiently high that the dominant cometary volatile (water ice, with latent heat $L \sim 2 \times 10^6$ J kg^{-1}) begins to sublimate. The resulting comae lead to a relabeling of the objects as Jupiter family comets (JFCs).

Objects evolving between the Kuiper Belt and JFC populations are collectively known as Centaurs (prototype object (2066) Chiron; Kowal et al. 1979). Their most important dynamical characteristic is that Centaurs experience strong and frequent gravitational deflections by the major planets, causing them to be dynamically short-lived. The mean half life is ∼3 Myr according to Horner et al. (2004b), and ∼7 Myr according to Tiscareno & Malhotra (2003), but with a wide range from 1 to 100 Myr. No single definition of the Centaurs exists. We favor the practical definition that Centaurs are objects that have semimajor axes $a < a_N$ and perihelia, q, in the range of $a_J < q < a_N$, where $a_J = 5.2$ au and $a_N = 30$ au are the semimajor axes of Jupiter's and Neptune's orbits, provided they are not trapped in mean-motion resonances with the giant planets (Jewitt 2009). Others (e.g., Horner et al. 2004a) relax the semimajor axis limit, noting that the dynamical character is essentially unchanged whether the object crosses Neptune's orbit or not. By these relaxed standards various Kuiper Belt objects, specifically the Neptune-crossers in the scattered disk population, are included.

2060 Chiron (Kowal et al. 1979) is widely regarded as the prototype Centaur (strangely ignoring 29P/Schwassmann–Wachmann 1, which also has a perihelion outside Jupiter's orbit, a semimajor axis smaller than Neptune's, and which was discovered four decades before Chiron). 29P/Schwassmann–Wachmann 1 is continuously active, driven by the sublimation of carbon monoxide at prodigious rates (Senay & Jewitt 1994; Womack et al. 2017). Chiron displays a (transient) dust coma (Hartmann et al. 1990; Luu & Jewitt 1990; Meech & Belton 1990) and evidence of CN gas emission (Bus et al. 2001). Comet-like activity has subsequently proved to be a feature of many members of the Centaur population (Jewitt 2009). Activity beyond Jupiter suggests the sublimation of more volatile (lower latent heat) ices, but other physical processes may play a role. Abundant ices present in comets include CO, CO_2, and less abundant N_2, all of which are

volatile at temperatures found in the giant planet region of the solar system and which are, presumably, present in Centaurs. Indeed, direct detection of CO gas has been made in Centaur 29P/Schwassmann–Wachmann 1 ($q = 5.7$ au; Senay & Jewitt 1994; Festou et al. 2001; Gunnarsson et al. 2008) and weak CO emission has also been reported in 174P/Echeclus ($q = 5.8$ au; Wierzchos et al. 2017) as well as Chiron ($q = 8.5$ au; Womack & Stern 1999). On the other hand, CO has not been detected in most of the Centaurs in which it was sought (Bockelee-Morvan et al. 2001; Jewitt et al. 2008; Drahus et al. 2017).

A clue about the nature of distant activity is provided by the observation that the known active Centaurs have perihelia $q \lesssim 10$ au, corresponding roughly to the orbit of Saturn, while Centaurs with larger perihelia appear inactive (Jewitt 2009). This radial segregation is intriguing because supervolatile sublimation should proceed strongly out to much larger distances (>30 au, in case of CO). The free sublimation of CO and other supervolatile ices offers no reason to expect the cessation of cometary activity at distances beyond ~10 au.

The crystallization of amorphous water ice offers a more natural, but unproved, explanation for the activation of distant objects near 10 au. The timescale for crystallization is an extremely strong function of temperature, and hence of heliocentric distance, given by

$$\tau_{\rm cr}(T) = 3.0 \times 10^{-21} \exp\left[\frac{E_A}{kT}\right] \quad (1)$$

where E_A is the activation energy, k is Boltzmann's Constant, and $E_A/k = 5370$ K (Schmitt et al. 1989). For example, at the subsolar point on an object at 10 au the crystallization timescale (decades) is comparable to the orbit period while at 30 au it is longer than the age of the solar system (Jewitt 2009; Guilbert-Lepoutre 2012). Crystallization, in addition to being exothermic, triggers the expulsion of trapped molecules, including supervolatile species (Bar-Nun et al. 2007). The mass loss in this hypothesis is still driven by the expansion of the suddenly freed supervolatiles, but their rate of release is, somewhat counter-intuitively, controlled by the thermodynamics of water ice. For this reason, the distance and temperature dependence of activity driven by crystallization is distinct from that of freely sublimating supervolatile ices.

Figure 1 shows solutions to Equation (1) for two limiting cases of the surface temperature on a uniform, spherical body. The lowest possible radiative temperature corresponds to the isothermal case, when power from the Sun is absorbed on one hemisphere but radiated uniformly from the entire surface. The corresponding isothermal blackbody temperature is $T_{\rm BB} = 278 r_{\rm H}^{-1/2}$. The highest local temperature is found at the subsolar point on a non-rotating body, and can be shown to equal $T_{\rm SS} = 2^{1/2} T_{\rm BB}$. Low and high-temperature solutions to Equation (1) are shown in the figure as dashed red and solid blue lines, respectively. We also show the Keplerian orbit period versus $r_{\rm H}$ as a thick black line. Points A and B mark the intersections of the curves and set the outer limits of the zones in which crystallization can occur on timescales comparable to the orbit period, for the low and high-temperature cases. The figure shows that crystallization can occur out to 14 au, an inference confirmed by more sophisticated numerical calculations (Guilbert-Lepoutre 2012).

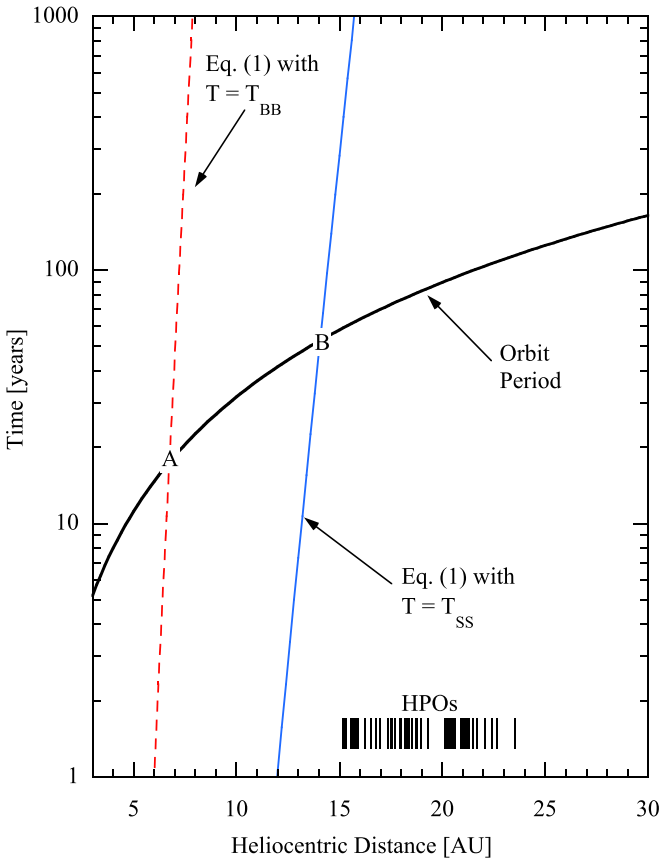

Figure 1. Crystallization timescale (Equation (1)) as a function of heliocentric distance and two limiting temperature models. The dashed red curve corresponds to the spherical blackbody temperature (i.e., the low temperature limit) while the solid blue curve corresponds to the subsolar temperature on a non-rotating nucleus. The solid black curve shows the Keplerian orbit period. Points A and B mark the inner and outer bounds of the region in which crystallization is expected. The "bar code" at the bottom shows the perihelion distances of the 53 HPOs in our sample; all are more distant from the Sun than point B.

The crystallization hypothesis is attractive because laboratory experiments (e.g., Zheng et al. 2009) clearly show that the amorphous state is the natural state for ice accreted at low temperatures and pressures, as existed in the Sun's protoplanetary disk. While physically plausible and widely assumed (Prialnik 1997), evidence for the existence of amorphous ice in solar system bodies is limited. Proof of the abundance of amorphous ice would be scientifically valuable because, if the Centaurs are amorphous, then so must be their precursors in the Kuiper Belt. The amorphous/crystalline state of Kuiper Belt ice in turn affects our understanding of the formation, composition, and thermal evolution of these objects.

These considerations motivate the present study, in which we use the high-resolution imaging capabilities of the Hubble Space Telescope (HST) to undertake a sensitive search for activity in high-perihelion objects. We reason that the detection of activity in objects with perihelia far beyond the crystallization distance would invalidate the hypothesis, and thus offer a scientifically useful, observational test.

2. Observations

We employed the 2.4 m diameter HST for its superb angular resolution and sensitivity to near-nucleus dust. Our observations were taken under the Cycle 25 "SNAP" proposal GO

15344 using the Wide Field Camera 3 (WFC3). WFC3 employs two 2000×4000 pixel charge-coupled devices (CCDs) with an image scale of $0\farcs04$ pixel^{-1}, giving a field of view of $162'' \times 162''$ and a Nyquist-sampled resolution of $0\farcs08$. We read out only half of one of the CCDs in order to optimize the observing efficiency and we used the F350LP filter because it is broad (FWHM $\sim$ 4758 Å) and offers a high throughput needed to identify the faint coma. The effective central wavelength of F350LP, when used to observe a Sun-like (G2V) spectrum, is $\lambda_c = 6230$ Å. For each target, we obtained two consecutive images of 300 s duration with the telescope tracked to follow the motion of the target.

2.1. The Sample

Our sample includes a broad mixture of classical Centaurs ($a_J < q < a_N$ and $a < a_N$) and Neptune-crossing Kuiper Belt objects ($a_J < q < a_N$, any a). We refer to these collectively as high-perihelion objects (HPOs). All HPOs were required to have $15 < q < 30$ au, comfortably larger than the $\sim$10 au distance out to which activity has so far been detected, and to have ephemeris uncertainties $\leqslant 10''$ (obtained from the JPL Horizons website[6]) at the time of observation. A total of 53 HPOs were successfully observed. Their orbital elements are listed in Table 1 in ascending order of the perihelion distance, q. Figure 1 shows the perihelia as short black lines, all clearly more distant from the Sun than the high-temperature critical point B.

Figure 2 shows the object distribution in the semimajor axis versus eccentricity plane, with Trans-Neptunian objects (TNOs, combining the classical and resonant population) plotted as orange circles,[7] and Centaurs and scattered objects as yellow circles.[8] Red diamonds in Figure 2 represent active Centaurs studied by Jewitt (2009) and Guilbert-Lepoutre (2012). Blue circles represent our HPO sample. Four black curves show the loci of orbits having perihelion distances equal to the aphelia of Jupiter, Saturn, Uranus, and Neptune, marked *J*, *S*, *U*, and *N*, respectively. Figure 3 shows the perihelion versus inclination plane, with the same color coding as in Figure 2. These two figures show that our sample occupies a wide range of semimajor axes and inclinations, consistent with the Neptune-scattered objects, all with perihelion distances larger than 15 au, but smaller than 30 au.

2.2. Photometry

Cosmic rays are abundant in HST data, and so we developed a scheme for their removal. First, the two images of each object were registered and then subtracted from each other. In the resulting difference images, most pixels have values close to zero except where cosmic rays fall in either image. Next, we determined the distribution of pixel differences and applied a sigma cutoff to identify cosmic-ray contaminated pixels, which we replaced with the local average value. The entire image plane was treated in this way, except that a circular region 10 pixels in radius and centered on the object was excluded in order to prevent accidental replacement of the real signal. Such special treatment can leave cosmic rays within the central area unaffected. In these rare cases, and where possible, we manually removed the cosmic rays from the area by interpolation. Figure 4 shows a sample image, with inset boxes showing the region around the target both before and after cosmic-ray removal. More than 70% of the targets have two

Table 1
Orbital Parameters Sorted by Perihelion Distance

Object		q[a]	a[b]	e[c]	i[d]
#	Name	(au)	(au)		
	(2014 JG80)	15.175	21.286	0.287	32.8
471272	(2011 FY9)	15.184	59.366	0.744	37.8
87555	(2000 QB243)	15.209	34.667	0.561	6.8
341275	(2007 RG283)	15.292	20.007	0.236	28.8
	(2014 FB72)	15.557	23.865	0.348	17.0
523753	(2014 WV508)	15.597	55.330	0.718	21.2
	(2013 UR15)	15.686	56.019	0.720	22.3
	(2010 LO33)	15.686	22.852	0.314	17.9
	(2013 PU74)	15.796	33.626	0.530	12.7
523746	(2014 UT114)	15.886	30.385	0.477	15.2
523720	(2014 LN28)	16.264	35.988	0.548	8.7
514312	(2016 AE193)	16.522	31.356	0.473	10.2
523673	(2013 MZ11)	16.765	24.169	0.306	6.4
523719	(2014 LM28)	16.771	262.038	0.936	84.8
	(2015 BF515)	16.970	20.423	0.169	28.3
	(2014 GQ53)	17.377	25.317	0.314	22.8
42355 Typhon	(2002 CR46)	17.512	37.784	0.537	2.4
44594	(1999 OX3)	17.572	32.263	0.455	2.6
	(2007 BP102)	17.722	23.938	0.260	64.8
	(2014 JE80)	17.934	90.071	0.801	28.2
	(2014 XQ40)	18.000	68.667	0.738	14.7
471149	(2010 FB49)	18.192	22.546	0.193	24.4
	(2012 GU11)	18.203	182.852	0.900	10.7
523686	(2014 DB143)	18.293	20.148	0.092	21.3
	(2014 NX65)	18.394	22.828	0.194	11.4
	(2013 CE223)	18.513	21.898	0.155	5.2
	(2005 UN524)	18.740	21.640	0.134	17.8
	(2010 WG9)	18.759	53.833	0.652	70.2
523710	(2014 JF80)	18.764	33.656	0.442	13.8
523709	(2014 JD80)	18.982	25.239	0.248	39.1
471513	(2012 CE17)	18.985	21.578	0.120	5.9
	(2013 RG98)	19.284	23.243	0.170	46.0
	(2008 AU138)	20.128	32.323	0.377	42.8
463368	(2012 VU85)	20.209	29.407	0.313	15.0
	(2013 FN28)	20.331	35.542	0.428	8.6
	(2011 FX62)	20.367	48.256	0.578	18.2
	(2006 UX184)	20.423	38.195	0.465	37.4
33128	(1998 BU48)	20.523	33.382	0.385	14.2
	(2004 VM131)	20.630	67.839	0.696	14.1
	(2002 PQ152)	20.894	25.754	0.189	9.3
	(2013 UE15)	20.907	60.806	0.656	6.7
127546	(2002 XU93)	20.981	67.390	0.689	77.9
501214	(2013 TC146)	21.006	25.164	0.165	14.2
316179	(2010 EN65)	21.066	30.785	0.316	19.2
	(2008 KV42)	21.171	41.858	0.494	103.5
	(2014 SB349)	21.220	25.845	0.179	15.5
	(2014 GP53)	21.290	26.772	0.205	14.3
	(2013 MY11)	21.511	51.646	0.583	14.5
	(2010 TV191)	21.694	24.856	0.127	11.5
471155	(2010 GF65)	22.096	33.266	0.336	12.4
	(2004 MW8)	22.414	33.524	0.331	8.2
	(2014 GR53)	22.634	212.236	0.893	42.1
160427	(2005 RL43)	23.546	24.614	0.043	12.3

Notes.
[a] Perihelion distance.
[b] Semimajor axis.
[c] Orbital eccentricity.
[d] Orbital inclination in degrees.

[6] https://ssd.jpl.nasa.gov/horizons.cgi
[7] https://www.minorplanetcenter.net/iau/lists/TNOs.html
[8] https://www.minorplanetcenter.net/iau/lists/Centaurs.html

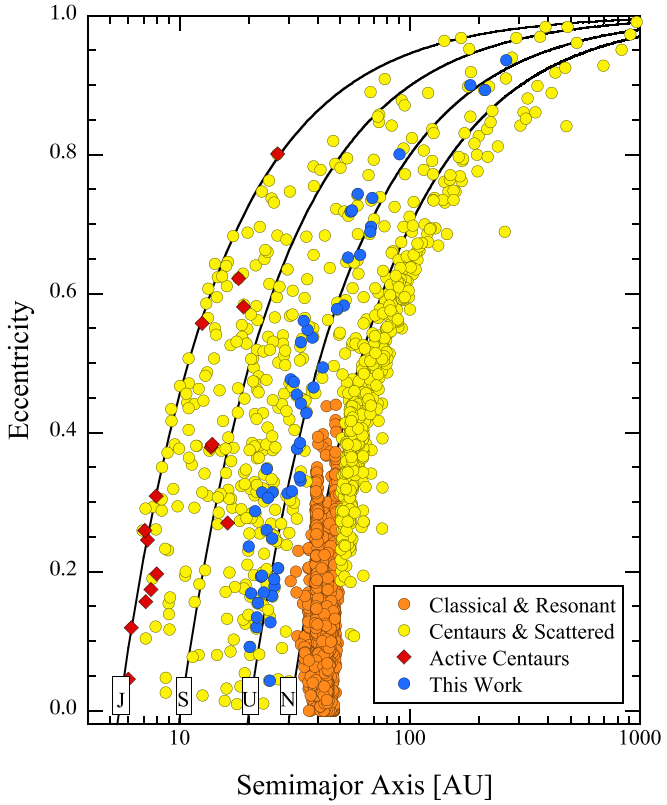

Figure 2. Orbital eccentricity as a function of the semimajor axis. Colors represent different classes of objects. Centaurs observed in this SNAP/HST program are plotted as filled blue circles. The classical and resonant Kuiper Belt objects are in orange circles and Centaurs including scattered Kuiper Belt objects are in yellow circles. They are found in the Minor Planet Center website: https://minorplanetcenter.net/iau/mpc.html. Active Centaurs (red diamonds) are from Jewitt (2009) and Guilbert-Lepoutre (2012). Solid curves show the loci of orbits having aphelion distances at Jupiter ($Q = 5.46$ au), Saturn ($Q = 10.12$ au), Uranus ($Q = 20.11$ au), and Neptune ($Q = 30.33$ au).

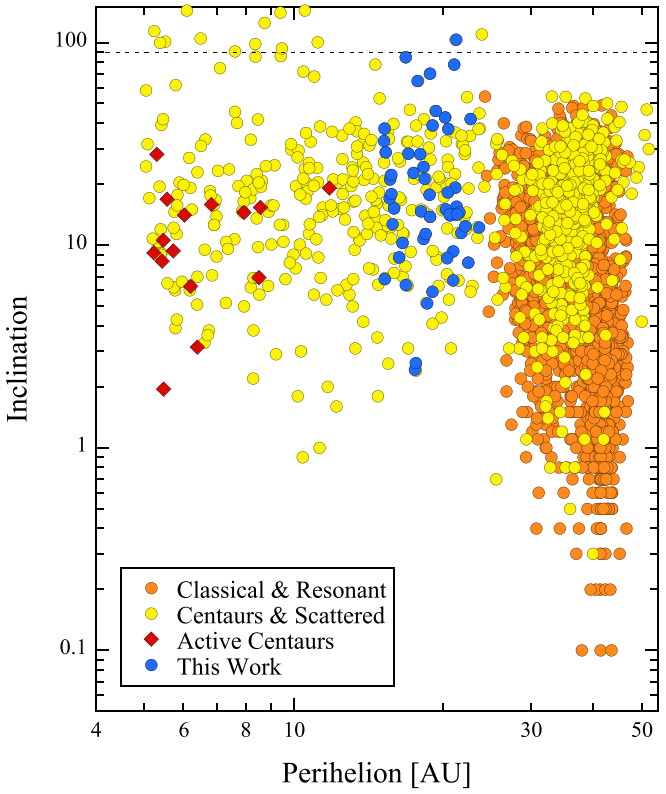

Figure 3. Orbital inclination as a function of the perihelia. Different object classes are color coded as in Figure 2. Objects above the dashed horizontal line are retrograde (inclination $i > 90°$). Concentration of active objects with $q \lesssim 10$ au is evident.

useful observations and we present the average of the two measurements in this paper. In the remaining cases, cosmic rays unfortunately overlap the target in one of the two images, but in no case were both images so affected. Where necessary, we report data using only a single image. As a test, we compared photometry from the automatically cosmic-ray cleaned images with photometry from images in which cosmic rays were removed manually, finding no significant differences. We used the photometry from the automated technique in our analysis.

We successfully observed 53 HPOs. The brightness of the nucleus was measured using an extraction aperture 0.″2 (5 pixels, see the innermost green circle in Figure 4) in radius. The sky background was determined in a concentric ring with inner and outer radii of 0.″8 and 4.″0 (20–100 pixels). The outmost green circle is the 20 pixel radius in Figure 4. We converted the apparent magnitudes from instrument magnitudes assuming HST calibration to a solar-type (G2V) spectrum. Table 2 lists the observed objects with their observing date UT, heliocentric and geocentric distances, phase angle, and measured apparent magnitude (V).

Figure 5 compares the apparent magnitudes, V, with predicted values listed on the JPL Horizons site, $V_{\rm JPL}$. The solid straight line shows $V = V_{\rm JPL}$. A majority of the target

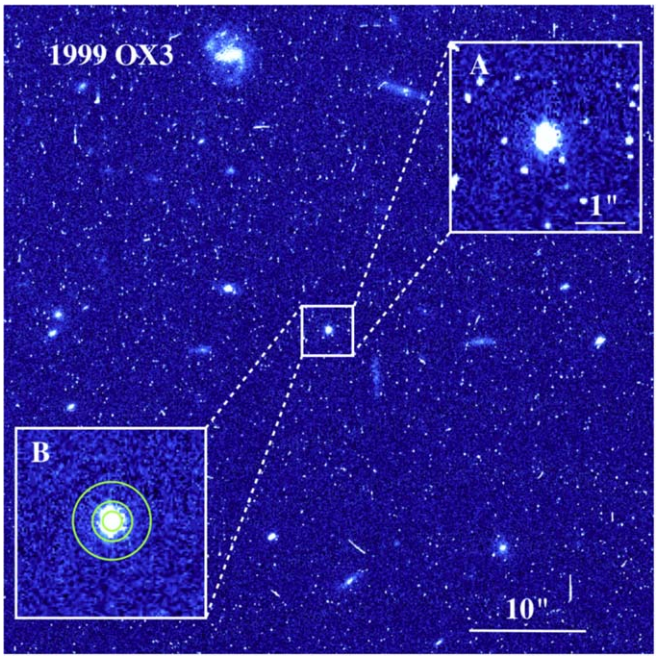

Figure 4. Single 300 s integration HST image of 1999 OX3 at $r_{\rm H} = 18.5$ au, shown with a logarithmic stretch between data numbers −0.08 and 0.15. Panel (A) is a zoomed-in box to show the immediate vicinity of the Centaur. Panel (B) shows the same region as panel (A), cleaned of cosmic rays, and with green circles marking the 0.″2, 0.″4, and 0.″8 radius (corresponding to 5, 10, and 20 pixels) photometry apertures.

Table 2
Centaur Observations in Chronological Order

Object		Date (UT)[a]	r_H[b] (au)	Δ[c] (au)	α[d]	V[e]
#	Name					
	(2006 UX184)	2017 Oct 20	20.445	19.651	1.7	22.07
523753	(2014 WV508)	2017 Oct 20	15.879	16.083	3.5	21.91
	(2004 MW8)	2017 Oct 21	26.345	26.045	2.1	22.92
	(2008 AU138)	2017 Oct 30	44.079	44.149	1.3	23.44
	(2013 UE15)	2017 Nov 1	21.959	21.131	1.5	22.34
523746	(2014 UT114)	2017 Nov 11	16.182	15.247	1.2	20.84
341275	(2007 RG283)	2017 Nov 16	15.769	14.924	1.9	20.69
	(2014 SB349)	2017 Dec 3	23.778	22.937	1.3	23.35
471513	(2012 CE17)	2017 Dec 7	18.976	19.127	2.9	22.23
	(2013 UR15)	2017 Dec 12	17.978	17.230	2.1	23.71
501214	(2013 TC146)	2017 Dec 13	26.600	27.127	1.8	21.06
	(2010 TV191)	2017 Dec 15	27.989	27.056	0.6	22.81
	(2004 VM131)	2017 Dec 16	31.421	30.448	0.3	23.21
	(2015 BF515)	2017 Dec 17	17.745	16.935	1.9	22.41
	(2010 WG9)	2017 Dec 19	23.056	22.083	0.4	21.71
	(2013 RG98)	2017 Dec 20	21.842	21.269	2.1	22.75
	(2005 UN524)	2017 Dec 31	18.744	17.798	0.8	22.06
	(2007 BP102)	2018 Jan 13	18.732	19.031	2.8	23.55
523719	(2014 LM28)	2018 Feb 1	16.773	17.161	3.1	22.47
	(2014 JE80)	2018 Feb 13	17.978	18.413	2.8	22.81
	(2014 GR53)	2018 Feb 16	22.634	22.565	2.5	21.90
	(2002 PQ152)	2018 Feb 18	23.652	24.088	2.1	23.49
	(2008 KV42)	2018 Feb 25	26.604	26.523	2.1	23.26
	(2013 FN28)	2018 Mar 1	20.331	19.508	1.6	21.83
471272	(2011 FY9)	2018 Mar 4	19.879	19.312	2.4	22.13
	(2014 FB72)	2018 Mar 18	17.887	17.294	2.6	21.21
463368	(2012 VU85)	2018 Mar 21	24.413	24.572	2.3	22.89
471149	(2010 FB49)	2018 Apr 11	26.435	25.440	0.3	21.53
523709	(2014 JD80)	2018 Apr 12	19.692	20.023	2.7	22.45
127546	(2002 XU93)	2018 Apr 14	23.564	23.539	2.4	21.94
42355 Typhon	(2002 CR46)	2018 Apr 15	21.606	20.615	0.4	21.14
	(2010 LO33)	2018 Apr 19	16.996	16.610	3.2	21.60
523686	(2014 DB143)	2018 Apr 30	19.385	18.580	1.8	21.96
	(2014 GQ53)	2018 May 7	19.055	18.149	1.4	22.29
44594	(1999 OX3)	2018 May 25	18.497	19.123	2.4	20.19
523720	(2014 LN28)	2018 Sep 13	17.254	16.363	1.6	20.78
33128	(1998 BU48)	2019 Mar 8	35.370	34.402	0.4	22.91
	(2013 CE223)	2019 Mar 9	23.847	22.859	0.3	22.60
160427	(2005 RL43)	2019 Mar 10	24.404	24.746	2.2	21.89
	(2014 XQ40)	2019 Mar 21	18.751	17.820	1.1	21.74
316179	(2010 EN65)	2019 Mar 29	26.955	25.990	0.6	21.45
	(2013 MY11)	2019 Apr 23	23.161	23.632	2.2	22.45
523673	(2013 MZ11)	2019 Apr 24	19.988	20.435	2.6	21.50
	(2014 GP53)	2019 May 3	21.860	20.889	0.7	22.40
	(2012 GU11)	2019 May 6	24.631	23.658	0.6	22.99
514312	(2016 AE193)	2019 May 20	17.359	17.630	3.2	21.14
	(2014 JG80)	2019 May 31	27.338	26.361	0.6	22.16
	(2013 PU74)	2019 May 31	16.416	16.798	3.2	22.72
87555	(2000 QB243)	2019 Jun 2	31.155	31.630	1.6	23.81
471155	(2010 GF65)	2019 Jul 2	23.192	22.347	1.4	21.04
	(2011 FX62)	2019 Aug 28	25.101	25.476	2.1	21.29
523710	(2014 JF80)	2019 Oct 3	18.776	17.890	1.4	21.69
	(2014 NX65)	2019 Oct 6	18.931	17.971	0.9	22.43

Notes.
[a] Observing date.
[b] Heliocentric distance.
[c] Geocentric distance.
[d] Phase angle.
[e] Apparent magnitude from $0\farcs2$ aperture.

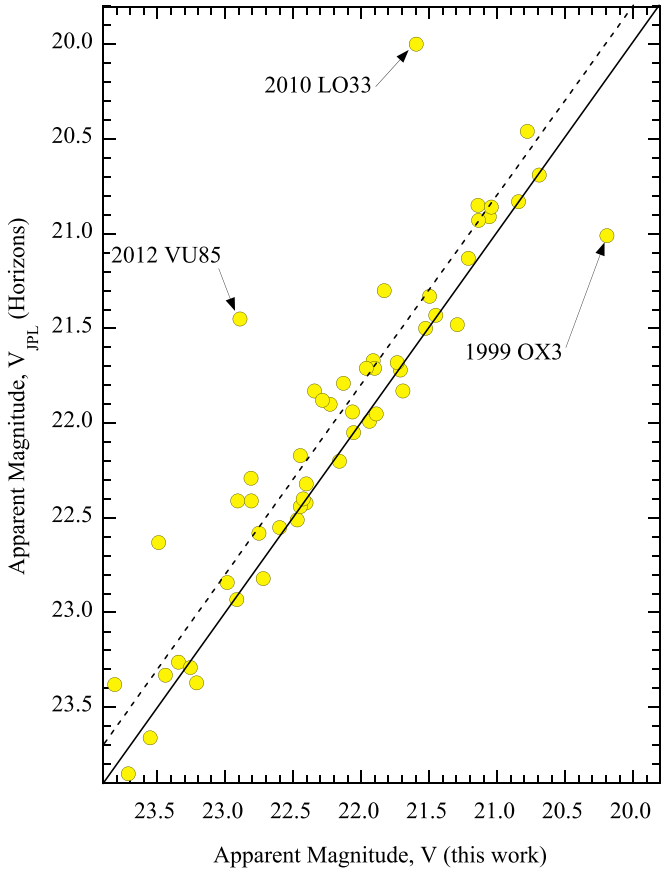

Figure 5. Comparison of apparent magnitudes, V, from the current work with those from the JPL Horizons database, $V_{\rm JPL}$. The solid line shows equal magnitudes, $V = V_{\rm JPL}$. The dashed line shows $V = V_{\rm JPL} + 0.20$.

objects are fainter than predicted by Horizons, in the sense $V = V_{\rm JPL} + 0.2$ (dashed line in Figure 5). This systematic offset is likely a result of a color term implicit in transforming the very broadband F350LP magnitudes to V. Remaining scatter about the dashed line is nearly symmetric and presumably caused by different objects having different phase functions (Bauer et al. 2013), and by rotational variations in the presented cross-sections, caused by aspherical shape. For a few objects (notably 1999 OX3, 2010 LO33, and 2012 VU85) the displacement from the dashed line is too large to be plausibly explained in this way, and the cause remains unknown.

We converted the apparent magnitudes to absolute magnitudes using

$$H_V = V - 5\log_{10}(r_{\rm H}\Delta) + 2.5\log_{10}(\Phi(\alpha)) \quad (2)$$

where $\Phi(\alpha) \leqslant 1$ is the phase function, equal to the ratio of the light scattered at phase angle α to that at $\alpha = 0°$, and $r_{\rm H}$ and Δ are the heliocentric and geocentric distances, respectively, both in astronomical units. The phase functions of Centaurs reported by Bauer et al. (2003) show a wide range, with G parameters from -0.13 to $+0.18$ in the HG system defined by Bowell et al. (1989). Similar diversity was reported by Rabinowitz et al. (2007), who also noted that the phase functions of Centaurs tend to be linear with α. Additional phase function measurements, also showing a wide scatter, are given in Alvarez-Candal et al. (2016) and Ayala-Loera et al. (2018). Motivated by these results, and in the interest of simplicity, we write $2.5\log_{10}(\Phi(\alpha)) = -\beta\alpha$, where $\beta = 0.061 \pm 0.002$ mag per degree is the mean value of the V-filter phase coefficients reported for seven Centaurs in Table 4 of Rabinowitz et al. (2007). Given that the maximum phase angles attained by the Centaurs in our sample are $\alpha_{\rm max} \sim 3°$ (Table 1), the necessary phase corrections are modest ($\beta\alpha_{\rm max} = 0.12$ mag). Uncertainties in the value of β render the derived absolute magnitudes uncertain by a similar amount. This is large compared to the photometric errors of the HST data, but comparable to or smaller than the likely variations in absolute magnitude caused by asphericity and rotation of the Centaurs. The apparent (V) and absolute magnitudes (H) are found in Tables 2 and 3, respectively. The absolute magnitudes as functions of the heliocentric distances are shown in Figure 6. As an example, 1999 OX3 is studied by others researchers. Our measurement, $H_V = 7.3$, is comparable to $H_R = 7.1$ reported by Bauer et al. (2003), but brighter than $H_V = 7.980 \pm 0.092$ and 7.60 ± 0.06 measured by Alvarez-Candal et al. (2016) and Ayala-Loera et al. (2018).

2.3. Effective Radii

To convert the magnitudes to effective radii, r_e, we use the relation

$$r_e = \left(\frac{1.5 \times 10^8}{p_V^{1/2}}\right) 10^{0.2(V_\odot - H)} \quad (3)$$

in which 1.5×10^8 is the number of kilometers in 1 au, $V_\odot = -26.74$ is the V-band magnitude of the Sun, and p_V is the geometric albedo.

As is true of the phase functions, the geometric albedos of most HPOs are unmeasured. The mean albedo of 52 Centaurs and scattered Kuiper Belt objects is $p_V = 0.08 \pm 0.04$ studied by Bauer et al. (2013), while the mean albedo of 16 Centaurs (in a largely overlapping object sample) reported by Duffard et al. (2014) is $p_V = 0.07 \pm 0.05$. The former authors also reported a color–albedo dependence, with blue objects having $p_V = 0.06 \pm 0.02$ and red objects $p_V = 0.12 \pm 0.05$ (see Figure 3 of Lacerda et al. 2014). However, it is worth noting that albedo determinations are difficult and the quoted uncertainties in some cases appear to underestimate the true uncertainties in the reported albedo. For example, 250112 (2002 KY14) was reported by Bauer et al. (2013) to have $p_V = 0.185 \pm 0.046$, a value that is three times larger than $p_V = 0.057^{+0.011}_{-0.007}$ as reported by Duffard et al. (2014). For simplicity, in this work we assume a nominal $p_V = 0.1$ for all objects in order to evaluate object dimensions on a uniform basis. Effective radii computed in this way can be easily scaled to other values of the albedo as they become available, in proportion to $(0.1/p_V)^{1/2}$ (Equation (3)). The effective radii of the Centaurs, computed from their apparent magnitudes using Equations (2) and (3), are listed in Table 3 and plotted against the perihelion distance in Figure 7. Evidently, the radii of most objects in our sample fall in the range of $10 \lesssim r_e \lesssim 100$ km, with a sample median of $r_e = 36$ km. We note that Bauer et al. (2003, 2013) gave the radii of Centaurs 1999 OX3 (~89 km), 2002 CR46 (85 ± 35 km), and 2002 XU93 (96 ± 35 km), all of which are comparable to our results (74, 57, and 52 km, respectively) within the uncertainties.

Table 3
Derived Quantities in Order of HPO Designated Names

Object		Date (UT)[a]	H_V[b]	r_e[c] (km)	C[d] (m^2)	M[e] (kg)	τ[f] (hr)	$\dot{M}$[g] (kg s^{-1})
33128	(1998 BU48)	2019 Mar 8	7.5	69	1.5×10^8	2.0×10^6	23.1	24
44594	(1999 OX3)	2018 May 25	7.3	74	4.3×10^7	5.7×10^5	12.8	12
87555	(2000 QB243)	2019 Jun 2	8.7	38	1.1×10^8	1.5×10^6	21.2	20
42355	(2002 CR46)	2018 Apr 15	7.9	57	1.3×10^8	1.7×10^6	13.8	34
127546	(2002 XU93)	2018 Apr 14	8.1	52	2.1×10^8	2.7×10^6	15.8	48
	(2002 PQ152)	2018 Feb 18	9.6	26	3.1×10^7	4.2×10^5	16.2	7
	(2004 MW8)	2017 Oct 21	8.6	40	3.3×10^7	4.4×10^5	17.5	7
	(2004 VM131)	2017 Dec 16	8.3	47	1.5×10^8	2.1×10^6	20.4	28
	(2005 UN524)	2017 Dec 31	9.4	28	1.7×10^7	2.3×10^5	11.9	5
160427	(2005 RL43)	2019 Mar 10	7.9	57	8.7×10^7	1.2×10^6	16.6	19
	(2006 UX184)	2017 Oct 20	8.9	35	8.7×10^7	1.2×10^6	13.2	24
	(2007 BP102)	2018 Jan 13	10.6	16	1.9×10^7	2.5×10^5	12.8	5
341275	(2007 RG283)	2017 Nov 16	8.7	38	2.1×10^7	2.8×10^5	10.0	8
	(2008 KV42)	2018 Feb 25	8.9	36	2.4×10^7	3.2×10^5	17.8	5
	(2008 AU138)	2017 Oct 30	6.9	88	1.3×10^8	1.8×10^6	29.6	17
471155	(2010 GF65)	2019 Jul 2	7.4	71	7.1×10^7	9.5×10^5	15.0	18
	(2010 WG9)	2017 Dec 19	8.2	50	7.8×10^6	1.0×10^5	14.8	2
316179	(2010 EN65)	2019 Mar 29	7.2	78	2.1×10^8	2.8×10^6	17.4	44
471149	(2010 FB49)	2018 Apr 11	7.4	71	5.4×10^3	7.2×10^1	17.1	1[h]
	(2010 TV191)	2017 Dec 15	8.4	45	9.2×10^7	1.2×10^6	18.2	19
	(2010 LO33)	2018 Apr 19	9.1	31	$10. \times 10^7$	1.3×10^6	11.2	33
471272	(2011 FY9)	2018 Mar 4	9.1	33	7.7×10^7	1.0×10^6	13.0	22
	(2011 FX62)	2019 Aug 28	7.1	80	9.0×10^7	1.2×10^6	17.1	19
463368	(2012 VU85)	2018 Mar 21	8.9	36	2.2×10^7	3.0×10^5	16.5	5
	(2012 GU11)	2019 May 06	9.1	32	9.0×10^7	1.2×10^6	15.9	21
471513	(2012 CE17)	2017 Dec 7	9.3	30	1.8×10^7	2.5×10^5	12.8	5
	(2013 MY11)	2019 Apr 23	8.6	40	2.8×10^7	3.7×10^5	15.9	6
	(2013 UE15)	2017 Nov 1	8.9	35	2.9×10^7	3.8×10^5	14.2	8
	(2013 RG98)	2017 Dec 20	9.3	30	3.0×10^7	4.0×10^5	14.3	8
	(2013 UR15)	2017 Dec 12	11.1	13	1.5×10^7	2.0×10^5	11.6	5
501214	(2013 TC146)	2017 Dec 13	6.7	99	4.2×10^8	5.6×10^6	18.2	85
	(2013 FN28)	2018 Mar 1	8.7	38	2.5×10^7	3.3×10^5	13.1	7
	(2013 PU74)	2019 May 31	10.3	18	1.4×10^7	1.8×10^5	11.3	5
523673	(2013 MZ11)	2019 Apr 24	8.3	47	8.6×10^8	1.1×10^7	13.7	231
	(2013 CE223)	2019 Mar 9	8.9	35	7.0×10^7	9.4×10^5	15.3	17
	(2014 NX65)	2019 Oct 6	9.7	24	3.5×10^7	4.7×10^5	12.1	11
523753	(2014 WV508)	2017 Oct 20	9.7	25	5.8×10^6	7.8×10^4	10.8	2
523746	(2014 UT114)	2017 Nov 11	8.8	37	6.4×10^6	8.5×10^4	10.2	2
	(2014 SB349)	2017 Dec 3	9.6	26	7.1×10^7	9.5×10^5	15.4	17
523719	(2014 LM28)	2018 Feb 1	10.0	21	2.0×10^7	2.7×10^5	11.5	6
	(2014 JE80)	2018 Feb 13	10.0	21	4.2×10^7	5.7×10^5	12.4	13
	(2014 GR53)	2018 Feb 16	8.2	49	4.4×10^7	5.9×10^5	15.1	11
	(2014 FB72)	2018 Mar 18	8.6	41	3.4×10^7	4.5×10^5	11.6	11
523709	(2014 JD80)	2018 Apr 12	9.3	29	4.5×10^7	6.0×10^5	13.4	12
523686	(2014 DB143)	2018 Apr 30	9.1	33	7.1×10^7	9.4×10^5	12.5	21
	(2014 GQ53)	2018 May 7	9.5	27	2.0×10^8	2.7×10^6	12.2	61
523720	(2014 LN28)	2018 Sep 13	8.4	44	2.7×10^7	3.6×10^5	11.0	9
	(2014 XQ40)	2019 Mar 21	9.0	33	5.1×10^6	6.8×10^4	12.0	2
	(2014 GP53)	2019 May 3	9.1	33	7.1×10^7	9.5×10^5	14.0	19
	(2014 JG80)	2019 May 31	7.8	58	2.6×10^7	3.5×10^5	17.7	5
523710	(2014 JF80)	2019 Oct 3	9.0	34	1.2×10^3	1.6×10^1	12.0	1[h]
	(2015 BF515)	2017 Dec 17	9.9	22	2.7×10^7	3.6×10^5	11.4	9
514312	(2016 AE193)	2019 May 20	8.5	42	3.3×10^7	4.5×10^5	11.8	10

Notes.
[a] Observing date.
[b] Absolute magnitude, computed from Equation (2).
[c] Nuclear radius, computed from Equation (3).
[d] Cross-section of dust projected within the aperture.
[e] Dust mass within aperture.
[f] Aperture residence time.
[g] Upper limit mass loss from Equation (12).
[h] Mass loss rate are rounded to 1.

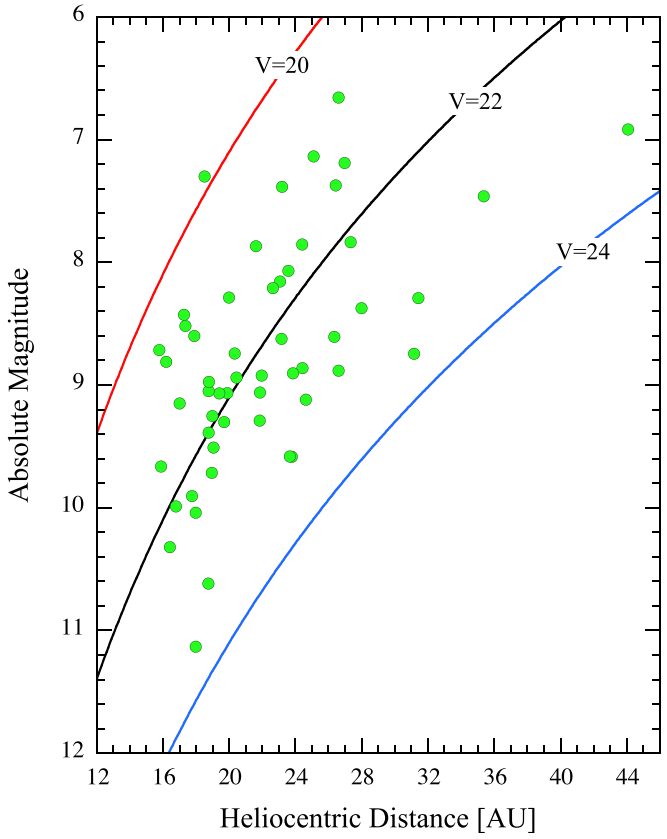

Figure 6. Absolute magnitude of the high-perihelion object (HPO) sample as a function of heliocentric distance. Lines show the apparent magnitudes, as labeled, for opposition observations (i.e., $\Delta = r_{\rm H} - 1$ and $\alpha = 0°$).

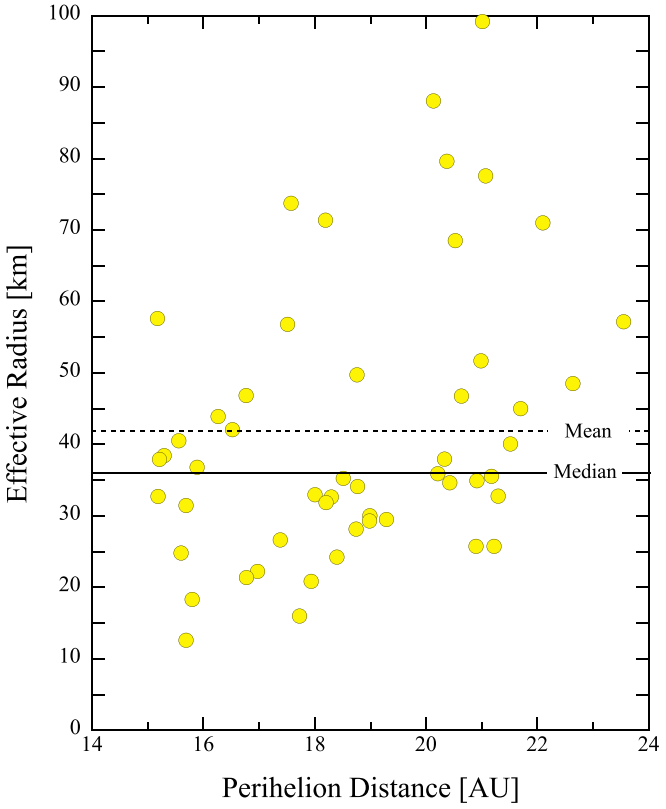

Figure 7. Effective radii, r_n, as a function of perihelion distance, q. Assuming $p_V = 0.1$, the median radius is $r_n = 36$ km (solid line) while the average radius is 42 km (dashed line).

2.4. Coma Detections

We search for coma by comparing annular photometry of the HPOs with reference stars measured identically. Stars in our HPO data set are all trailed by the nonsidereal motion of HST. Instead, to obtain an empirical measure of the point-spread function (PSF) we used the profiles of reference stars in untrailed (i.e., sidereal target) archival WFC3 images taken through the F350LP filter with comparable integration times. We used the HST archive to identify 27 stars free from confusion with nearby stars and galaxies, and which have apparent magnitudes similar to those of the HPO sample. The average surface brightness profiles derived from the stars and the HPOs are compared in Figure 8, showing good agreement within the uncertainties of measurement. The HST observations provide no evidence that the HPOs, as a group, exhibit coma.

Next, we use aperture photometry as the primary means to quantify the presence of coma in individual objects. This technique is robust, simple to apply and to interpret, and, given the narrow and stable PSF of the HST, is also very sensitive. A significant advantage is that the technique is independent of the morphology assumed by the ejected dust, whether it be spherically symmetric or highly collimated into a tail or trail by the action of solar radiation pressure. We base our analysis on Jewitt (2009), with small modifications described below.

All targets and point sources (stars) were measured using three concentric apertures of radii (see the green circles in Figure 4) $\theta_0 = 0\farcs2$ (5 pixels), $\theta_1 = 0\farcs4$ (10 pixels), and $\theta_2 = 0\farcs8$ (20 pixels), yielding the three apparent magnitudes, V_0, V_1, and V_2. Note that V_0 is the nucleus magnitude.

We define the annular magnitude excess as

$$\Delta V_{i,j} = (V_i - V_j)_{\rm HPO} - \overline{(V_i - V_j)_\star} \quad (4)$$

where the aperture pairs are $i, j = (0, 1), (0, 2)$, and $(1, 2)$. Subscripts "HPO" and "$\star$" refer to the high-perihelion object and the star profiles. The average, median, and standard deviations of quantities $(V_i - V_j)_{\rm HPO}$ and $(V_i - V_j)_\star$ are listed in Table 4. The mean and median quantities are equal within the uncertainties. Note that all entries are consistent with $\Delta V_{i,j} = 0$ at the 3σ level. For reference, we also measured in the same way a synthetic image created using the TinyTim simulation software (Krist et al. 2011). This image gave results slightly different from the empirical determinations listed in Table 4 (e.g., $(V_1 - V_2)_\star = 0.034$ versus 0.048 from the table) and we elected to use the empirical determinations over those from TinyTim.

Figure 9 shows $\Delta V_{1,2}$ as a function of the V magnitude for stars (yellow circles) and HPOs (green circles). For the stars, we replaced $(V_i - V_j)_{\rm HPO}$ in Equation (4) with the individual aperture difference for each star. Gray squares with error bars show the mean and standard deviation of $\Delta V_{1,2}$ within a series of magnitude bins each 0.5 mag wide. The scatter of the measurements clearly grows as the objects become fainter, from ± 0.006 mag at $V = 20.25$ to ± 0.040 at $V = 23.75$. Curved lines in the figure show a model of the uncertainty incorporating both photon (Poisson) noise and CCD readout noise. For the latter, we assumed the canonical WFC3 values for readout noise =3 electrons, digitization at 1.5 electrons per analog-to-digital unit (ADU), and that a $V = 0$ source gives

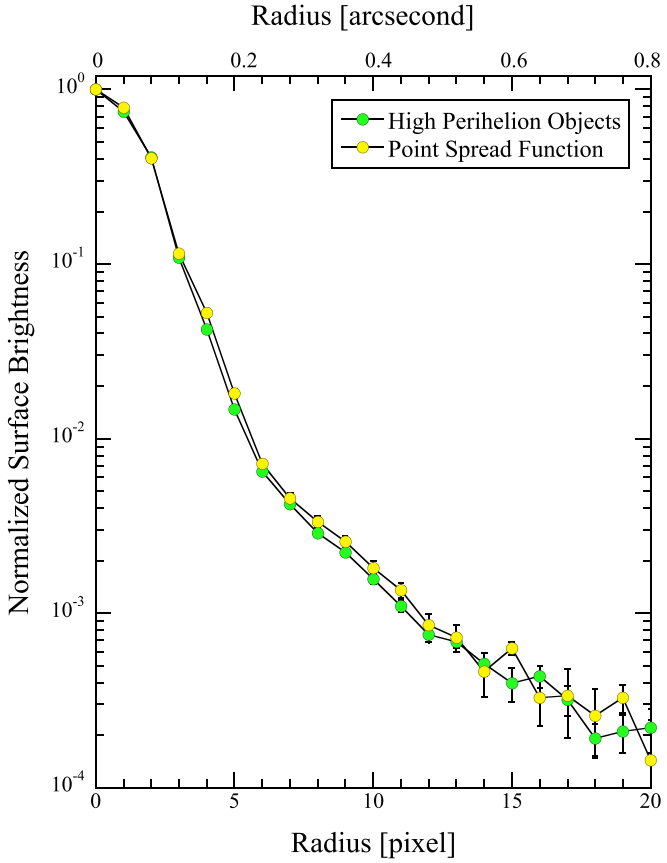

Figure 8. Normalized mean radial surface brightness profiles of high-perihelion objects (HPOs, green filled circles) and stars (yellow filled circles) with error bars computed from the standard deviations of 53 object and 27 stellar profiles.

4.72×10^{10} ADU s^{-1}. We also used the measurement, from stars, that 4.8% of the light from a point source falls in the annulus between a 10 and 20 pixel radius. The agreement between the model and actual uncertainties gives us confidence that the data are essentially photon limited, and therefore of very high quality.

The cumulative distribution of $\Delta V_{1,2}$ is displayed in Figure 10, where $\overline{(V_i - V_j)_\star} = 0.051$ (see Table 4). All but two HPOs have $\Delta V_{1,2} < 0.03$. The $\Delta V_{1,2}$ Gaussian best-fit distribution has a $\sigma = 0.042$ centered at -0.007. Within the uncertainties, the brightness enhancement around the HPOs is zero, indicating that comae of HPOs are not detected.

2.5. Mass-loss Rates

We derive upper limits to the mass loss from measured upper limits to the coma. The mass of a collection of spherical particles can be written as

$$M = \int_{a_0}^{a_1} \frac{4}{3}\pi\rho a^3 n(a)da. \quad (5)$$

Here, ρ is the particle density and $n(a)da$ is the differential size distribution, equal to the number of particles with radii between a and $a + da$, and distributed in the range of $a_0 \leqslant a \leqslant a_1$. It is convenient to assume a power-law size distribution, $n(a)da = \Gamma a^{-\gamma}da$, where Γ and γ are constants. The total cross-section of the particles is

$$C = \int_{a_0}^{a_1} \pi a^2 n(a)da. \quad (6)$$

Equations (5) and (6) can be combined to give

$$M = \frac{4}{3}\rho\bar{a}C \quad (7)$$

for all $\gamma \neq 3$ or 4, where $\bar{a}$ is the average particle radius. We adopt $\gamma = 3.5$, based on measurements of comets (Grün et al. 2001), for which $\bar{a} = \sqrt{a_0 a_1}$. We adopt $a_0 = 0.1\,\mu$m, since smaller particles are inefficient optical scatterers and contribute little to the scattered light intensity. The appropriate value of a_1 is less certain. Since we are mainly interested in scaling from one object to the next, we adopt $a_1 = 1$ mm, giving $\bar{a} = 10\,\mu$m. Then, Equation (7) allows us to calculate the particle mass corresponding to the cross-section inferred from the photometry.

Equation (7) gives the particle mass projected within an annulus around the nucleus. The approximate residence time of particles in the annulus is

$$\tau = \frac{\Delta r}{U} \quad (8)$$

where U (m s^{-1}) is the average speed of the particles leaving the nucleus. The width, Δr, is related to the angular dimensions of the annulus by

$$\Delta r = s\delta\theta\Delta \quad (9)$$

where $\delta\theta = \theta_j - \theta_i$ is in arcseconds, Δ is in astronomical units, and scale factor $s = 7.25 \times 10^5$ m arcsec^{-1} au^{-1} is the number of meters in one arcsecond at one astronomical unit.

The particle speed, U, in Equation (8) is unmeasured. Practical lower and upper limits to U are set by the gravitational escape speed and the gas sound speed, respectively. The escape speed, for a sphere of radius r_e and density ρ_n is given by

$$V_e = \left(\frac{8\pi G\rho_n}{3}\right)^{1/2} r_e \quad (10)$$

where $G = 6.67 \times 10^{-11}$ N kg^{-2} m^2 is the gravitational constant. With $\rho_n = 1000$ kg m^{-3} and r_e in kilometers, Equation (10) gives $V_e = 0.75 r_e$ (m s^{-1}). At the median radius $r_e = 36$ km, the typical escape speed is $V_e = 27$ (m s^{-1}).

The gas sound speed is

$$V_{\rm th} = \left(\frac{8kT}{\pi\mu m_h}\right)^{1/2} \quad (11)$$

where $k = 1.38 \times 10^{-23}$ J K^{-1} is Boltzmann's constant, T is the gas temperature, μ is the molecular weight of the gas, and $m_{\rm H} = 1.67 \times 10^{-27}$ kg is the mass of the hydrogen atom. As previously noted, water ice does not sublimate appreciably at the large heliocentric distances considered here and only super-volatiles constitute plausible sources of gas drag. We solved the energy balance equation for sublimating CO ($\mu = 28$) to find that the equilibrium sublimation temperature is negligibly dependent on heliocentric distance (we find $T = 26.6$ K at $r_{\rm H} = 5$ au falling to $T = 24.4$ K at 30 au) as a result of the dominance of the latent heat term in the energy balance. We take $T \sim 25$ K, giving $V_{\rm th} = 120$ m s^{-1}. This is consistent with thermal broadening of CO rotational lines in distant bodies (e.g., Senay & Jewitt 1994

Table 4
Statistics of Coma Measurements

(i, j)[a]	Radii		$(V_i - V_j)_{\rm HPO}$	$(V_i - V_j)_\star$	$\Delta V_{i,j}$[b]
0, 1	0.″2–0.″4	Mean	0.095 ± 0.004	0.085 ± 0.003	0.010 ± 0.005
		Median	0.088	0.082	0.006
0, 2	0.″2–0.″8	Mean	0.145 ± 0.005	0.136 ± 0.005	0.009 ± 0.007
		Median	0.138	0.127	0.011
1, 2	0.″4–0.″8	Mean	0.050 ± 0.004	0.051 ± 0.004	−0.001 ± 0.006
		Median	0.046	0.048	−0.002

Notes.
[a] Annuli.
[b] Excess magnitude from Equation (4).

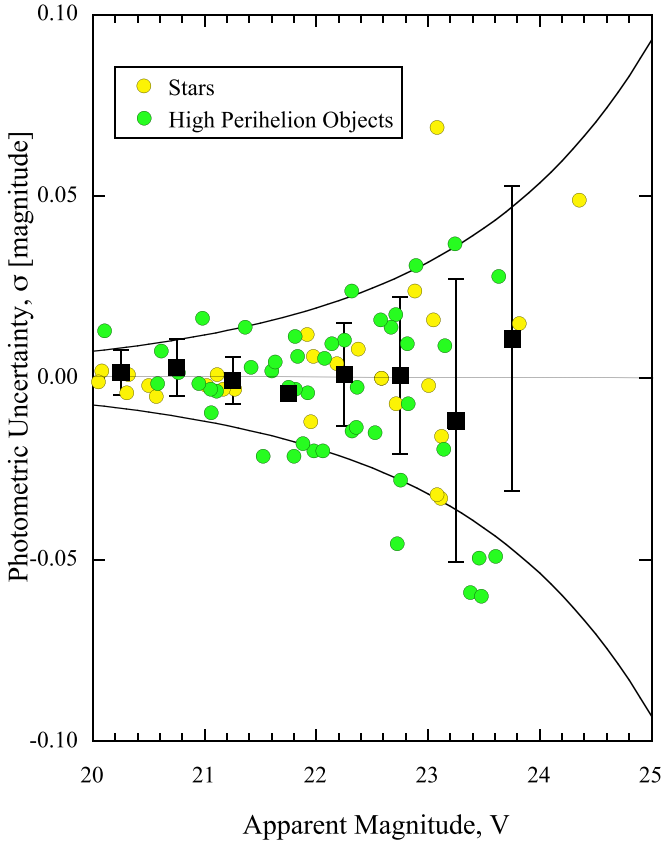

Figure 9. Uncertainties in the measured annular magnitudes as a function of the source brightness. Yellow and green symbols distinguish HPOs from field stars. The curved lines show the expected noise based on a model. Gray squares show the mean and ±1 standard deviation within a series of apparent magnitude bins each 0.5 mag wide. The concordance between the actual scatter and the expected uncertainties shows that the WFC3 data are photometrically well behaved.

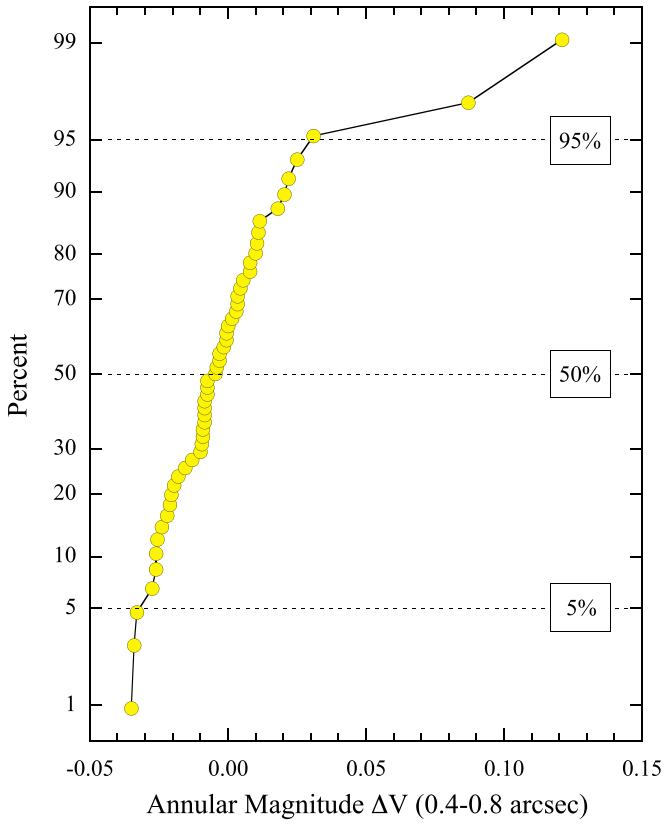

Figure 10. Cumulative distribution of annular magnitudes $\Delta V_{1,2}$ ($\theta = 0.''4$–$0.''8$). Dashed horizontal lines mark the 5%, 50%, and 95% values, as labeled.

measured a CO line width of $\sim$200 m s^{-1} in 29P when at $r_{\rm H} = 6$ au, while Crovisier et al. 1995 independently measured 140 m s^{-1} in the same object).

Even for the largest objects in our sample (see Table 3), we find $V_{\rm th} > V_e$, consistent with the gas drag expulsion of particles.[9] Finally, the mass-loss rate, $\dot{M} \sim M/\tau$, is obtained by combining Equations (7)–(9) to find

$$\frac{dM}{dt} = \frac{4}{3}\left(\frac{\rho \bar{a} C}{s \delta \theta \Delta}\right) U. \quad (12)$$

Since $\dot{M} \propto U$, and we are interested in setting upper limits to the mass loss, we set $U = V_{\rm th} = 120$ m s^{-1} in Equation (12). The resulting mass-loss rates are listed in the last column in Table 3. In the table, Centaurs are listed in order of their designated names.

3. Discussion

Figure 11 shows the derived mass-loss rates as a function of the perihelion distance, with downward-pointed filled yellow triangle symbols used to indicate the upper limits. The figure shows that no activity was detected in any of the HPOs

[9] As an aside, we note from Equations (10) and (11) that $V_{\rm th} = V_e$ when $r_e = 160$ km. In all larger objects, gas drag will be unable to eject even the smallest particles against self-gravity and only suborbital dust trajectories will result. The scattering cross-section and time-dependent brightness of such a body could still be affected by dust but no resolved comae would be present. None of the objects in our sample are this large.

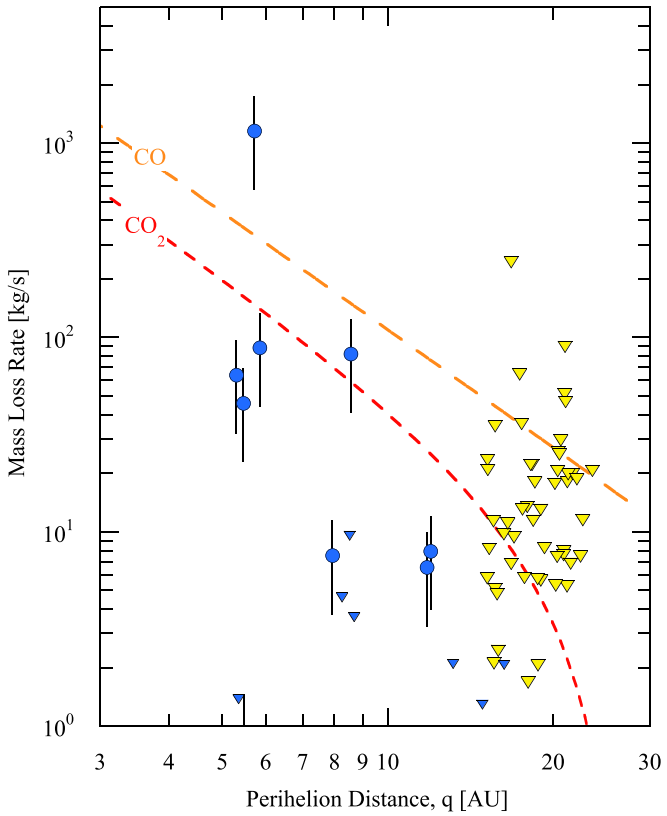

Figure 11. Mass-loss rate vs. perihelion distance. Yellow filled triangles indicate upper limits from this work. Blue symbols denote data from Jewitt (2009), with circles indicating detections and triangles indicating upper limits. Error bars on the blue circle detections are added to represent a factor of two uncertainties. The orange and red dashed lines show solutions to Equation (13) for CO and CO_2 ices, respectively, with exposed surface areas of 5 km^2.

observed in the present study. The (model-dependent) mass-loss limits range from ~2 to ~10^2 kg s^{-1}, depending on the size and distance to each object. The median limiting mass-loss rate in the HPO sample is $\dot{M} < 11$ kg s^{-1} and the median perihelion distance is $q = 19$ au.

For comparison, we include in Figure 11 estimates of $\dot{M}$ from Jewitt (2009) obtained using ground-based telescopes on a selection of Centaurs having (mostly) smaller perihelion distances than in our current sample. In order to permit direct comparison with the HST measurements we have scaled the $\dot{M}$ values from column 9 of their Table 4 to the same particle size, $\overline{a} = 10$ μm, as used here. Nondetections are again indicated by (blue) downward pointing triangles while coma detections are marked with blue filled circle symbols and error bars equal to a factor of two in the production rates. The median mass-loss rate and perihelion distance of the active Centaurs are 46 kg s^{-1} and 5.8 au, respectively. Other measurements of Centaurs reported by Cabral et al. (2019) refer to objects close to the limiting magnitude of their survey. They have negligible sensitivity to extended emission from outgassing and are not considered here.

Five of the eight active Centaurs in the Figure exhibit mass-loss rates large enough to have been detected in the HPO sample, had activity been present. In this sense, the nondetection of activity is consistent with the crystallization hypothesis, which predicts that no examples of activity should be found. Of course, while consistent, we cannot argue that the new data prove the crystallization hypothesis. This is because the sensitivity to coma achieved by HST is insufficient to rule out the presence of low-level supervolatile sublimation at 15 au and beyond.

To examine the nature of low-level activity at large r_H, we consider the energy balance for a sublimating surface, neglecting conduction, expressed as

$$\frac{L_\odot(1-A)}{4\pi r_H^2} = \chi[\varepsilon\sigma T^4 + f_s(r_H)L(T)]. \quad (13)$$

Here, A and ε are the Bond albedo and emissivity of the sublimating surface, $L_\odot$ is the solar luminosity, r_H is heliocentric distance expressed in meters, σ is the Stefan-Boltzmann constant, and $L(T)$ is the temperature-dependent latent heat of sublimation. Quantity f_s (kg m^{-2} s^{-1}) is the sublimation mass flux. We assume $A = 0.04$, $\varepsilon = 1$ while noting that solutions to Equation (13) are insensitive to both quantities provided $A \ll 1$ and $\varepsilon \gg 0$. Parameter χ is a dimensionless number that expresses the distribution of absorbed energy over the nucleus, varying between $\chi = 1$ for a flat surface oriented perpendicular to the Sun–comet line and $\chi = 4$ for an isothermal sphere. We adopt $\chi = 2$ as the intermediate case, corresponding to hemispheric warming of a spherical nucleus.

We solved Equation (13) using thermodynamic parameters for CO and CO_2 ices tabulated by Brown & Ziegler (1980). The results are plotted in Figure 11 where, for reference, we show the mass sublimated per second from an exposed 5 km^2 area of each ice (CO in orange, CO_2 in red). As noted above, the sublimation of CO declines closely as r_H^{-2} across the planetary region of the solar system while CO_2 exhibits a downturn beginning at about 15 au.

The observations set strong limits on the possible area of exposed supervolatiles on each object. For example, at the median perihelion distance $r_H = 19$ au, the equilibrium sublimation flux of CO from a flat surface oriented perpendicular to the Sun–object line is $f_s = 6 \times 10^{-6}$ kg m^{-2} s^{-1} (Equation (13)). Rate $\dot{M}$ then corresponds to sublimating area $A = f_s^{-1}\dot{M}$, assuming a gas-to-dust mass production rate of unity. The empirical median rate $\dot{M} < 11$ kg s^{-1} would reflect sublimation from an area $A < 2$ km^2. The implied active fraction is $f_A = A/(4\pi r_e^2)$, where $r_e = 36$ km is the median radius from Table 3. We obtain $f_A < 10^{-4}$, which is two to four orders of magnitude smaller than f_A measured on the nuclei of active JFCs (A'Hearn et al. 1995). Small values of f_A are to be expected since exposed CO sublimates rapidly even at 19 au ($f_s/\rho \sim 20$ cm yr^{-1}, or several meters per orbit).

We briefly discuss the distance-dependence of bias effects in imaging faint comae. First, the rate of supervolatile sublimation varies as r_H^{-2} (Figure 11). Scaling from median distance $q = 5.8$ au to 19 au, for example, corresponds to a sublimation rate smaller by a factor of ~11. Second, the dust comae are observed in reflected sunlight, the intensity of which also falls as r_H^{-2}, together giving an r_H^{-4} variation in the surface brightness of a coma at a fixed linear distance from an object sublimating in energy equilibrium with sunlight. Scaling from 5.8 to 19 au then corresponds to a fading of coma surface brightness by a factor ~115. This steep variation is partially offset by the improved angular resolution of HST, which allows for the measurement of any coma closer to the nucleus source (where the surface brightness is intrinsically higher, for a given mass-loss rate) than would be possible in ground-based, lower

resolution observations. Still, the bias against coma detection at large r_H remains, and low-level outgassing in the HPOs due to steady sublimation of exposed supervolatiles might be present but go unobserved.

3.1. Binary Fraction

Binaries are abundant in the Kuiper Belt; ~20% of the cold classical Kuiper Belt objects are binary, as are ~5% of the dynamically hot populations (Noll et al. 2008, 2019). Since the HPOs are products of the dynamically excited portion of the Kuiper Belt, it is reasonable to expect to find a binary fraction similar to the ~5% measured in the hot population. Currently, two binary Centaurs are known ((42355) Typhon I Echidna, Noll et al. 2006; and (65489) Ceto/Phorcys, Grundy et al. 2007). In our sample of 53 objects, for example, the expected number of binaries would be ~2.5. However, Brunini (2014) examined the disruptive effects of close planetary encounters on objects dipping into the giant planet region, finding that only about 10% of binaries should resist disruption over the long term. If applied to our sample of 53 objects, Brunini's fraction suggests that we should find an average of only 0.25 binaries.

The maximum separation for a binary to be stable against solar gravitational perturbations is given by the Hill radius, $r_{\rm Hill}$,

$$r_{\rm Hill} = q\left(\frac{\rho_n}{3\rho_\odot}\right)^{1/3}\left(\frac{r_n}{r_\odot}\right) \quad (14)$$

where q is the perihelion distance, $\rho_n = 1000\,{\rm kg\,m^{-3}}$ and $\rho_\odot = 1400\,{\rm kg\,m^{-3}}$ are the densities of the object and the Sun, respectively, and r_n and $r_\odot$ are the radius of the Centaur and the Sun. With $q \gg 1$ au, the angle subtended by the Hill radius is just $\theta_{\rm Hill} \sim r_{\rm Hill}/q$, which is expressed in arcseconds as

$$\theta_{\rm Hill} \sim 10''\left(\frac{r_n}{50{\rm km}}\right), \quad (15)$$

where r_n is radius in kilometers, independent of distance. In Equation (15) we have normalized to $r_n = 50$ km for convenience. The Nyquist-sampled (two pixel) WFC3 resolution of 0.″08 corresponds to $\sim 0.008\,\theta_{\rm Hill}$ for a 50 km radius object. Most resolved Kuiper Belt binaries occupy the central ~10% of the Hill sphere (Noll et al. 2019), corresponding to separations <1″, and still about 10 times the HST resolution.

We visually searched the Hill spheres of the target objects by comparing consecutive images to locate co-moving objects. Owing to asymmetries in the faint wings of the PSF, the sensitivity to binary companions is a complicated function of the component brightness ratio, the angular separation, and the position angle. It is therefore impossible to set a uniform limit to the presence of binary companions. Binaries with a large ratio of component brightnesses can easily escape detection and our search should therefore be understood to refer to binaries with equal-sized components, of which we detected none. The nondetection of binaries in the HPO sample sets a 3σ limit to the average binary fraction <8%, consistent with expectations above.

4. Summary

We used the HST to image 53 HPOs at ~0.″08 angular resolution. Objects in our sample were selected to have perihelion distances of $q > 15$ au, where subsolar radiation equilibrium temperatures are $T \lesssim 100$ K and amorphous water ice is too cold to crystallize on the orbital timescale.

1. No evidence for activity was found. We set upper limits to the mass loss, $\dot{M}$, from each object based on near-nucleus photometry and a simple model. At the median distance of our sample objects (19 au), the median value is $\dot{M} < 11\,{\rm kg\,s^{-1}}$, with an object-to-object range of $1 \lesssim \dot{M} \lesssim 231\,{\rm kg\,s^{-1}}$.
2. The nondetection of activity in our sample is consistent with the hypothesis that activity observed in dynamically similar objects having smaller perihelion distances is caused by the crystallization of amorphous ice.
3. Low-level activity due to equilibrium sublimation of exposed supervolatile ices cannot be excluded by our data. However, the fraction of the surface actively sublimating in equilibrium with sunlight must be $f_A \lesssim 10^{-4}$, reflecting the instability of supervolatiles even in the 19 au to 24 au range.
4. Our search yielded no binaries. Based on our sample and Poisson counting statistics, we conclude that the binary fraction is <8% (3σ). This is consistent with an origin of the HPOs in the dynamically hot population of the Kuiper Belt and binary disruption caused by interaction with the giant planets (Brunini 2014).

We thank the anonymous referee for the comments, specially on the phase coefficients. We are prompted to read the relevant papers which improve our understanding on the phase coefficients of centaurs. We thank Dr. Yoonyoung Kim for her discussions with us about the paper. Based on observations made under GO 15344 with the NASA/ESA Hubble Space Telescope, obtained at the Space Telescope Science Institute, operated by the Association of Universities for Research in Astronomy, Inc., under NASA contract NAS 5-26555.

ORCID iDs

Jing Li (李京) https://orcid.org/0000-0002-0982-7309
Max Mutchler https://orcid.org/0000-0002-0088-3021
Jessica Agarwal https://orcid.org/0000-0001-6608-1489

References

A'Hearn, M. F., Millis, R. C., Schleicher, D. O., Osip, D. J., & Birch, P. V. 1995, Icar, 118, 223
Alvarez-Candal, A., Pinilla-Alonso, N., Ortiz, J. L., et al. 2016, A&A, 586, A155
Ayala-Loera, C., Alvarez-Candal, A., Ortiz, J. L., et al. 2018, MNRAS, 481, 1848
Bar-Nun, A., Notesco, G., & Owen, T. 2007, Icar, 190, 655
Bauer, J. M., Grav, T., Blauvelt, E., et al. 2013, ApJ, 773, 22
Bauer, J. M., Meech, K. J., Fernández, Y. R., et al. 2003, Icar, 166, 195
Bockelee-Morvan, D., Lellouch, E., Biver, N., et al. 2001, A&A, 377, 343
Bowell, E., Hapke, B., Domingue, D., et al. 1989, in Asteroids II, ed. R. P. Binzel, T. Gehrels, & M. S. Matthews (Tucson, AZ: Univ. Arizona Press), 524
Brown, G., & Ziegler, W. 1980, Adv. Cryog. Eng., 25, 662
Brunini, A. 2014, MNRAS, 437, 2297
Bus, S. J., A'Hearn, M. F., Bowell, E., et al. 2001, Icar, 150, 94
Cabral, N., Guilbert-Lepoutre, A., Fraser, W. C., et al. 2019, A&A, 621, A102
Crovisier, J., Biver, N., Bockelee-Morvan, D., et al. 1995, Icar, 115, 213
Drahus, M., Yang, B., Lis, D. C., & Jewitt, D. 2017, MNRAS, 468, 2897
Duffard, R., Pinilla-Alonso, N., Santos-Sanz, P., et al. 2014, A&A, 564, A92
Festou, M. C., Gunnarsson, M., Rickman, H., Winnberg, A., & Tancredi, G. 2001, Icar, 150, 140
Grün, E., Hanner, M. S., Peschke, S. B., et al. 2001, A&A, 377, 1098
Grundy, W. M., Stansberry, J. A., Noll, K. S., et al. 2007, Icar, 191, 286

Guilbert-Lepoutre, A. 2012, AJ, 144, 97
Gunnarsson, M., Bockelée-Morvan, D., Biver, N., Crovisier, J., & Rickman, H. 2008, A&A, 484, 537
Hartmann, W. K., Tholen, D. J., Meech, K. J., et al. 1990, Icar, 83, 1
Horner, J., Evans, N. W., & Bailey, M. E. 2004a, MNRAS, 354, 798
Horner, J., Evans, N. W., & Bailey, M. E. 2004b, MNRAS, 355, 321
Jewitt, D. 2009, AJ, 137, 4296
Jewitt, D., Garland, C. A., & Aussel, H. 2008, AJ, 135, 400
Kowal, C. T., Liller, W., & Marsden, B. G. 1979, in Proc. IAU Symp. 81, Dynamics of the Solar System, ed. R. L. Duncombe (Dordrecht: Reidel), 245
Krist, J. E., Hook, R. N., & Stoehr, F. 2011, Proc. SPIE, 8127, 81270J
Lacerda, P., Fornasier, S., Lellouch, E., et al. 2014, ApJL, 793, L2
Luu, J., Marsden, B. G., Jewitt, D., et al. 1997, Natur, 387, 573
Luu, J. X., & Jewitt, D. C. 1990, AJ, 100, 913
Meech, K. J., & Belton, M. J. S. 1990, AJ, 100, 1323
Noll, K. S., Grundy, W. M., Chiang, E. I., et al. 2008, in The Solar System Beyond Neptune, ed. M. Barucci et al. (Tucson, AZ: Arizona Univ. Press), 345
Noll, K. S., Grundy, W. M., Grundy, W. M., & Thirouin, A. 2019, in The Trans-Neptunian Solar System, ed. D. Prialnik, M. Barucci, & L. Young (Amsterdam: Elsevier), 205
Noll, K. S., Levison, H. F., Grundy, W. M., et al. 2006, Icar, 184, 611
Prialnik, D. 1997, ApJL, 478, L107
Rabinowitz, D. L., Schaefer, B. E., & Tourtellotte, S. W. 2007, AJ, 133, 26
Schmitt, B., Espinasse, S., Grim, R. J. A., Greenberg, J. M., & Klinger, J. 1989, in Physics and Mechanics of Cometary Materials, ed. J. Hunt & T. Guyenne (Noordwijk: ESTEC), 65
Senay, M. C., & Jewitt, D. 1994, Natur, 371, 229
Tiscareno, M. S., & Malhotra, R. 2003, AJ, 126, 3122
Volk, K., & Malhotra, R. 2008, ApJ, 687, 714
Wierzchos, K., Womack, M., & Sarid, G. 2017, AJ, 153, 230
Womack, M., Sarid, G., & Wierzchos, K. 2017, PASP, 129, 031001
Womack, M., & Stern, S. A. 1999, SoSyR, 33, 187
Zheng, W., Jewitt, D., & Kaiser, R. I. 2009, JPCA, 113, 11174